

# A comparison of black hole growth in galaxy mergers with GASOLINE and RAMSES

J. M. Gabor<sup>1</sup>, Pedro R. Capelo<sup>2</sup>, Marta Volonteri<sup>3</sup>, Frédéric Bournaud<sup>1</sup>, Jillian Bellovary<sup>4</sup>, Fabio Governato<sup>5</sup>, and Thomas Quinn<sup>5</sup>

<sup>1</sup> CEA-Saclay, IRFU, SAp, F-91191 Gif-sur-Yvette, France

<sup>2</sup> Center for Theoretical Astrophysics and Cosmology, Institute for Computational Science, University of Zurich, Winterthurerstrasse 190, CH-8057 Zürich, Switzerland

<sup>3</sup> Institut d'Astrophysique de Paris, UMR 7095 CNRS, Université Pierre et Marie Curie, 98bis Blvd Arago, 75014 Paris, France

<sup>4</sup> Department of Astrophysics, American Museum of Natural History, Central Park West at 79th Street, New York, NY 10024, USA

<sup>5</sup> Astronomy Department, University of Washington, Box 351580, Seattle, WA, 98195-1580

August 30, 2021

## ABSTRACT

Supermassive black hole dynamics during galaxy mergers is crucial in determining the rate of black hole mergers and cosmic black hole growth. As simulations achieve higher resolution, it becomes important to assess whether the black hole dynamics is influenced by the treatment of the interstellar medium in different simulation codes. We here compare simulations of black hole growth in galaxy mergers with two codes: the Smoothed Particle Hydrodynamics code GASOLINE, and the Adaptive Mesh Refinement code RAMSES. We seek to identify predictions of these models that are robust despite differences in hydrodynamic methods and implementations of sub-grid physics. We find that the general behavior is consistent between codes. Black hole accretion is minimal while the galaxies are well-separated (and even as they “fly-by” within 10 kpc at first pericenter). At late stages, when the galaxies pass within a few kpc, tidal torques drive nuclear gas inflow that triggers bursts of black hole accretion accompanied by star formation. We also note quantitative discrepancies that are model-dependent: our RAMSES simulations show less star formation and black hole growth, and a smoother gas distribution with larger clumps and filaments, than our GASOLINE simulations. We attribute these differences primarily to the sub-grid models for black hole fueling and feedback and gas thermodynamics. The main conclusion is that differences exist quantitatively between codes, and this should be kept in mind when making comparisons with observations. However, reassuringly, both codes capture the same dynamical behaviours in terms of triggering of black hole accretion, star formation, and black hole dynamics.

**Key words.** Galaxies:active – Galaxies:evolution – Galaxies:formation – Galaxies:interactions – Galaxies:star formation

## 1. Introduction

Galaxy mergers are thought to be transformational events in galaxy evolution. Mergers transform stellar disks into spheroids (e.g. Toomre & Toomre 1972; Gerhard 1981; Negroponte & White 1983; Barnes & Hernquist 1996). Via tidal torques, they tend to compress gas into the central regions of galaxies, triggering powerful starbursts (e.g. Sanders et al. 1988; Barnes & Hernquist 1991; Mihos & Hernquist 1996). The increase in nuclear gas is further thought to fuel growth in galaxies’ central supermassive black holes, resulting in active galactic nuclei (AGNs, e.g. Sanders et al. 1988; Hernquist 1989; Di Matteo et al. 2005).

Correlations between supermassive black hole mass and global galaxy properties (see Kormendy & Ho 2013, and references therein) suggest a possible evolutionary link between black hole and galaxy growth (e.g. Silk & Rees 1998; Wyithe & Loeb 2003). The energetic output from AGNs may provide a physical driver for this link: in some cases, they emit sufficient energy to heat up all the cold gas in a galaxy, and they may trigger powerful outflows (e.g. Crenshaw et al. 2003; Di Matteo et al. 2005; Rupke & Veilleux 2011; Gabor & Bournaud 2014). AGNs sometimes power radio jets that can heat intergalactic and intracluster gas (e.g. Fabian et al. 2000; Voit & Donahue 2005; Randall et al. 2011). AGNs have been invoked in many mod-

els of galaxy evolution as a primary actor in regulating the star formation rates (SFRs) and stellar masses of the most massive galaxies (e.g. Hopkins et al. 2006; Croton et al. 2006; Somerville et al. 2008).

Numerical hydrodynamic simulations have led to many advances in our understanding of galaxy mergers and black hole fueling, but we have not yet developed a complete understanding of how results depend on details of these models. Different studies have used various treatments of hydrodynamics and feedback processes (such as supernova and AGN output), as well as different resolution. Details of the feedback treatment can have an important effect on black hole growth and its impact on galaxies (e.g. Debuhr et al. 2011; Wurster & Thacker 2013b,a; Newton & Kay 2013).

Differences in hydrodynamic method can also lead to differences in simulated galaxy (and inter-galactic) properties in various contexts. Recent work shows that Smoothed Particle Hydrodynamics (SPH; Lucy 1977; Gingold & Monaghan 1977), historically a commonly-used method in extragalactic astrophysics for solving the equations of hydrodynamics, is inaccurate in certain circumstances – for example in resolving shocks and Kelvin-Helmholtz and Rayleigh-Taylor instabilities (Agertz et al. 2007). Grid techniques, such as Adaptive Mesh Refinement (AMR; Berger & Colella 1989), generally improve upon these

problems (Agertz et al. 2007), but with drawbacks including advection errors, angular momentum conservation, and numerical diffusion (e.g. Wadsley et al. 2008; Hahn et al. 2010; see discussion and references in Hopkins 2014). More recent hybrid techniques employing a moving mesh (Springel 2010) or no mesh at all (Hopkins 2014) help resolve these difficulties.

In cosmological simulations, traditional SPH as implemented in the `GADGET` code (Springel 2005) tends to allow a smaller quantity of gas to cool and fuel galaxies than mesh-based codes, leading to smaller gas disks (Kereš et al. 2012; Vogelsberger et al. 2012; Scannapieco et al. 2012). The apparently suppressed cooling in SPH relative to moving mesh methods also allows the formation of more prominent hot halos in idealized merger simulations, along with clumps and filaments in those halos (Hayward et al. 2014). This is true despite the fact that, in cosmological SPH simulations, a smaller proportion of gas accreting onto galaxies passes through a hot phase (Nelson et al. 2013). (Note that recent improvements to SPH have helped alleviate many of these discrepancies; e.g. Beck et al. 2015 and references therein. Such improvements have recently been implemented in `GASOLINE` as described in e.g. Keller et al. 2014.) Despite these important differences, it appears that differences in feedback implementations cause more prominent changes than differences in the numerical method for hydrodynamics (Scannapieco et al. 2012). Moving forward, large code-comparison projects like `AGORA` (Kim et al. 2014) should help elucidate these issues in the context of galaxy evolution. With the exception of Hayward et al. (2014), the impact of different codes and numerical techniques on supermassive black hole fueling and feedback has scarcely been studied.

In this work, we compare high-resolution simulations of black hole growth in galaxy mergers with two codes: the `GASOLINE` SPH code, and the `RAMSES` AMR code. While many authors have used SPH codes to study black holes in idealized galaxy mergers, relatively few have used AMR codes (see e.g. Kim et al. 2011). We use standard physical recipes in both codes for star formation, black hole growth, and stellar and black hole feedback. In §2 we describe the simulations. Then we highlight similarities and differences, and attempt to explain them, in §3. We conclude in §4.

## 2. Simulations

For our analysis, we focus on four representative simulations of galaxy mergers: two run with `GASOLINE` and two with `RAMSES`. The merging galaxies have mass ratios of 2:1 and 4:1, gas fractions of 30%, and disks oriented coplanar with their orbits. We have also run some resolution tests and simulations with other mass ratios and orbital configurations (see Capelo et al. 2015), which give similar results. Below we describe numerical details of the `GASOLINE` simulations – including details of the initial conditions – then those of the `RAMSES` simulations.

### 2.1. Methods: `GASOLINE`

We use a subset of the suite of `GASOLINE` merger simulations described fully in Capelo et al. (2015). We summarize the simulations here. `GASOLINE` (Wadsley et al. 2004), an N-body SPH code, is based on `PKDGRAV` (Stadel 2001), which uses a tree method to calculate gravitational dynamics among particles. We note that these simulations do not include recent improvements in the SPH method (Keller et al. 2014).

As a Lagrangian particle code, the resolution is automatically adaptive – the highest resolution occurs in the densest regions.

Dark matter particles, initial star particles, and initial gas particles have masses of  $1.1 \times 10^5 M_\odot$ ,  $3.3 \times 10^3 M_\odot$ , and  $4.6 \times 10^3 M_\odot$  (respectively), with softening lengths of 30 pc, 10 pc, and 20 pc (respectively).

`GASOLINE` includes models for gas cooling, star formation, supernovae and stellar winds, and black hole accretion and feedback. The simulations use a standard model for gas cooling, which incorporates metal cooling but no heating by a UV radiation background (Shen et al. 2010). A temperature floor of 500 K is imposed.

Star formation occurs as a random process (see Katz 1992) in gas particles colder than 6000 K and denser than 100 particles  $\text{cm}^{-3}$ . The SFR is calculated by assuming that a fraction  $\epsilon_* = 1.5\%$  of the eligible gas forms into stars per star formation time, where the star formation time is the greater of the gas free fall time or the gas cooling time. With a probability consistent with the star formation rate and timestep, a star-forming gas particle will convert some of its mass into a collisionless star particle.

Stellar feedback includes a blast wave model for Type II supernovae (Stinson et al. 2006). In this model, supernova energy is calculated based on the mass of young stars that should explode, and this energy is distributed (as thermal energy) among gas particles that are neighbors of the star particle. To mimic an expanding blast wave, gas cooling is turned off for a time that depends on the local gas conditions and the feedback energy.

Nuclear black holes are treated as sink particles that accrete surrounding gas (Bellovary et al. 2010). The accretion rate onto the black hole is calculated separately for each neighbor gas particle based on a Bondi accretion rate (cf. Bondi 1952), and the sum of the rates from each gas particle yields the total accretion rate. Mass is then removed from the gas particles in proportion to their contribution to the accretion rate, and the mass is added to the black hole. We note that the Bondi accretion rate here includes a boost factor of  $\alpha = 3$  (see Booth & Schaye 2009 for a discussion of boost factors). The accretion rate is capped at  $\alpha$  times the Eddington Limit. A fixed fraction  $\epsilon_r = 0.1$  of the accreted mass-energy is emitted as radiation at each timestep, and a coupling fraction  $\epsilon_f = 0.001$  of the radiated energy injected as thermal energy into the nearest gas particle.

#### 2.1.1. `GASOLINE` simulation set up and initial conditions

We set up mergers of two disk galaxies as in Capelo et al. (2015). Galaxies begin with parabolic orbits (Benson 2005), initial separations the sum of the two galaxies' virial radii, and separation at first pericenter equal to 20% of the virial radius of the larger galaxy (Khochfar & Burkert 2006). The galactic disks are coplanar with their orbits, and both galaxies rotate in the same direction as the orbit (prograde-prograde mergers).

Each galaxy is modeled as a dark matter halo, stellar bulge, stellar disk, and gaseous disk (Springel & White 1999; Springel et al. 2005), plus a supermassive black hole. The dark matter halo follows an NFW (Navarro et al. 1996) profile up to the virial radius, with an exponential decay beyond. It has spin parameter  $\lambda = 0.04$  and concentration  $c = 3$ . The stellar bulge makes up 0.8% of the virial mass, and follows a Hernquist (1990) profile. The galactic disk makes up 4% of the virial mass, and follows an exponential surface density profile. The disk scale radius is derived from conservation of angular momentum of the material making up the disk. Thirty percent of the disk mass is gas, so that the fraction of total baryons in gas (the common observational definition of gas fraction) is  $0.3(0.04M_{\text{vir}})/(0.04M_{\text{vir}} + 0.008M_{\text{vir}}) = 0.25$ . Supermassive black holes with masses  $2 \times 10^{-3}$  times the bulge mass (Marconi & Hunt 2003) are placed

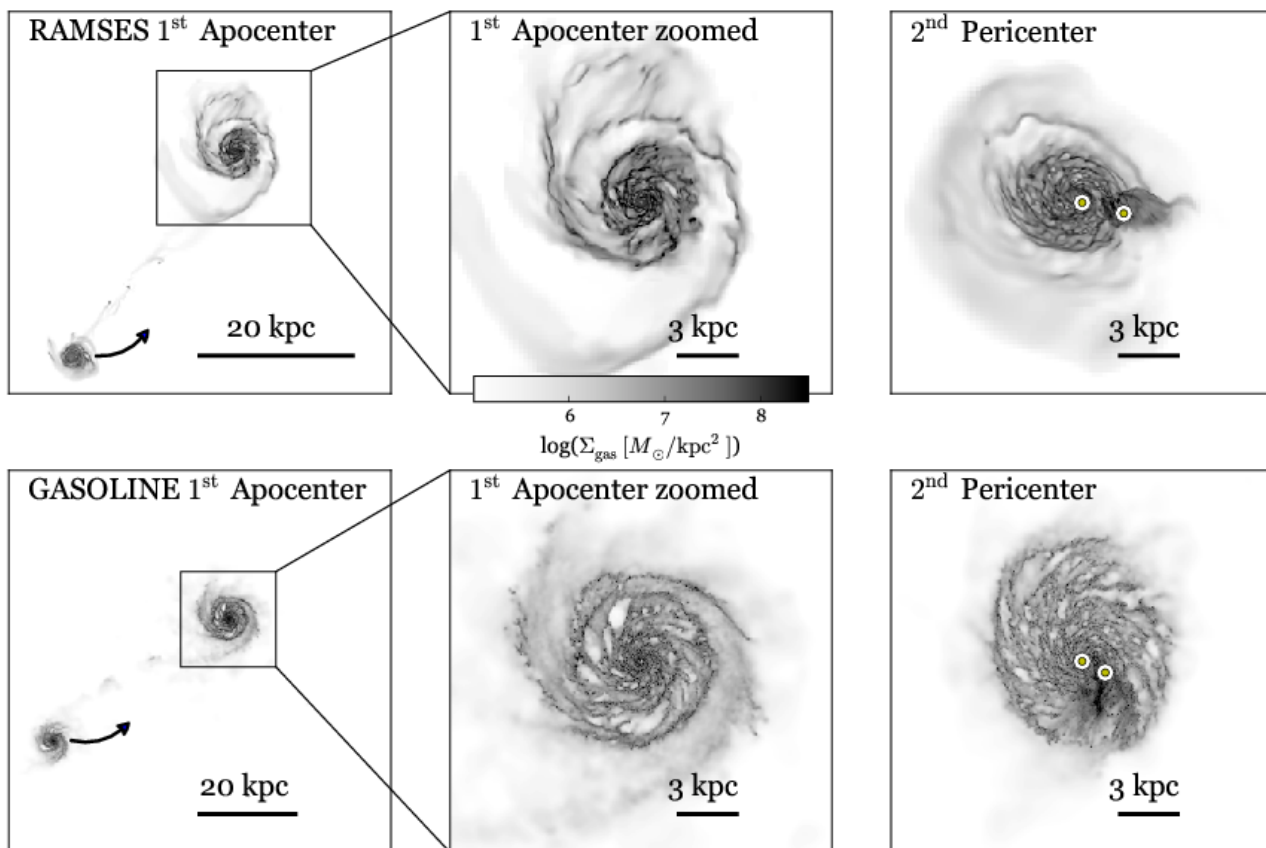


**Fig. 1.** Snapshots showing gas surface density for our 4:1 RAMSES (**top**) and GASOLINE (**bottom**) simulations. **Left** panels show both galaxies at first apocenter, with arrows roughly indicating the direction of travel of the secondary galaxy. **Middle** panels show a zoom-in on the primary galaxy at first apocenter, and **right** panels show both galaxies at second pericenter. In the right panels, circles mark the positions of the black holes (in each simulation, the more massive black hole is to the left).

at the centers of initialized galaxies. In each simulation, the primary galaxy has a virial mass of  $2.21 \times 10^{11} M_{\odot}$ , bulge mass  $1.77 \times 10^9 M_{\odot}$ , disk mass  $8.83 \times 10^9 M_{\odot}$ , and disk scale radius of 1.13 kpc. The secondary galaxies have their masses scaled down by factors of two and four, respectively.

Model galaxies undergo a relaxation period of 100 Myr in isolation before they begin the merger. During this period, the star formation efficiency  $\epsilon_*$  is gradually increased to its final value, 1.5%, to prevent unphysical bursts of supernova feedback. After this relaxation, the supermassive black hole masses are reset to their initial values, and the galaxies are placed in appropriate orbits for the mergers.

## 2.2. Methods: RAMSES

We have run a small new suite of merger simulations using the RAMSES AMR code (Teyssier 2002). Our set up borrows many aspects from Gabor & Bournaud (2013, 2014) and Perret et al. (2014), and mostly uses standard recipes for physical processes. RAMSES solves the equations of hydrodynamics on the mesh, while it treats collisionless matter (dark matter and stars) as particles. The effects of gravity are calculated on the mesh using a multigrid method, and particle accelerations are interpolated using a cloud-in-cell method.

We use the standard quasi-lagrangian mesh refinement criteria: a cell is refined if it contains  $> 30$  dark matter particles, or if the mass in the cell exceeds  $5 \times 10^3 M_{\odot}$ . In addition, we refine cells whose mass is sufficiently large that the local gas Jeans

length is not resolved by at least 4 cell widths (Truelove et al. 1997). These refinement criteria ensure that the highest resolution is applied to the densest regions, where star-forming clouds form. We allow refinement up to level 15, corresponding to a minimum cell size of about 7.6 pc (with a box side length of 250 kpc).

The thermodynamics is treated with a standard model for gas cooling, including metal cooling (e.g. Teyssier et al. 2013). We impose an overall temperature floor of 100 K, as well as a density-dependent temperature floor (the Jeans polytrope) that ensures the local Jeans length in the smallest grid cells is always resolved by at least 4 cells (Machacek et al. 2001). The Jeans polytrope acts as an additional pressure (or pressure floor) that prevents numerical fragmentation. The normalization of this temperature floor depends on resolution, and is higher for lower resolution simulations.

RAMSES includes models for star formation and supernova feedback. Star formation occurs as a random process in cells whose gas (particle number) density exceeds  $100 \text{ H atoms cm}^{-3}$ . In cells above this threshold density, a fraction  $\epsilon_* = 1$  per cent of the gas is assumed to form into stars per free fall time, yielding an SFR for each cell. A new collisionless star particle is created in the cell with a probability based on the SFR and the timestep. New star particles inherit the position and velocity of the gas cell out of which they formed, but they are decoupled and will generally move into other cells.

After a delay of 10 Myr, supernovae explode at the locations of newly formed star particles. Twenty per cent of the mass of

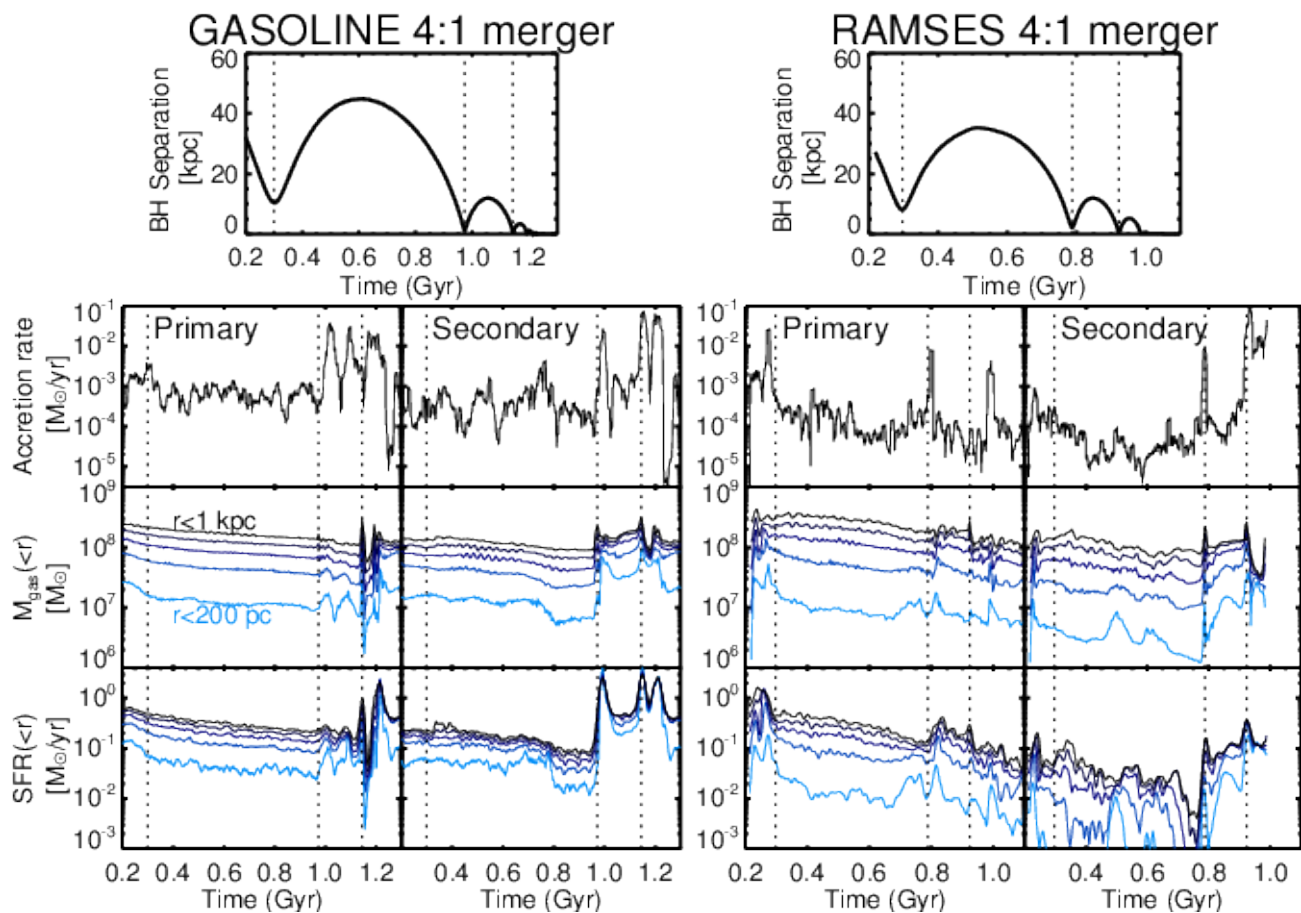


**Fig. 2.** BH separation in kpc (top), black hole accretion rate (BHAR) in  $M_{\odot} \text{ yr}^{-1}$  (second row), gas mass in  $M_{\odot}$  within spheres up to 1 kpc in radius (third row), and SFR in  $M_{\odot} \text{ yr}^{-1}$  within the same spheres (bottom row) vs. time for a 4:1 merger with GASOLINE (left) and RAMSES (right). For each simulation, we show quantities for the primary galaxy/BH on the left, and the secondary galaxy/BH on the right. We show gas masses and SFRs within radii of 200 pc to 1 kpc, in increments of 200 pc. Quantities are smoothed on 10 Myr timescales. Note that time-axes differ by  $\sim 20\%$  (see §3.2.1). Vertical dotted lines mark local minima in the separation between the two black holes in all panels. The GASOLINE and RAMSES simulations show qualitatively similar results: enhanced accretion and star formation rates at second pericenter, and especially at 3rd pericenter/coalescence.

the initial star particle is assumed to explode as supernovae, and for each  $10 M_{\odot}$  of exploding supernova,  $10^{51}$  ergs of thermal energy is added to the hosting cell. Following Stinson et al. (2006) and Teyssier et al. (2013), cooling is delayed for 20 Myr in the supernova-heated cell to enable more efficient feedback.

Supermassive black holes are represented by collisionless sink particles. The sink particles accrete gas according to a Bondi accretion rate (cf. Bondi 1952), where the gas density and temperature are computed from a weighted average of all gas cells within  $4\Delta x$  (where  $\Delta x$  is the smallest cell size, Krumholz et al. 2004). We use the standard Bondi formula, without a “boost” factor  $\alpha$  (Booth & Schaye 2009). The accretion rate is capped at the Eddington limit, assuming a radiative efficiency  $\epsilon_r = 0.1$ . Black hole particles merge once they pass within  $4\Delta x$  of one another.

Black hole feedback is implemented as a thermal deposition of energy (Dubois et al. 2010; Teyssier et al. 2011). A fraction  $\epsilon_r = 0.1$  of the accreted mass is assumed to convert into radiative energy, and a fraction  $\epsilon_e = 0.15$  of the radiative energy is assumed to couple to the surrounding gas as thermal heating (Booth & Schaye 2009; Dubois et al. 2010; Teyssier et al. 2011). Following Booth & Schaye (2009), we only inject AGN feedback energy if it is sufficient to heat the surrounding gas to  $T_{\text{min,AGN}} = 10^7$  K. This prevents the deposited energy from being

immediately radiatively cooled from dense gas, leading to more efficient feedback. On timesteps where the feedback energy is insufficient to heat the gas to  $T_{\text{min,AGN}}$ , we store the feedback energy to be added to that during the following timesteps. This storage is repeated until enough energy is stored to reach  $T_{\text{min,AGN}}$ , at which time it is released. We deposit the feedback energy in gas cells within  $4\Delta x$  with a weighting where colder, denser gas acquires more of the energy (Gabor & Bournaud 2013). If the post-injection gas temperature would exceed  $T_{\text{max,AGN}} = 5 \times 10^9$  K, then we iteratively expand the injection radius by 25 per cent to dilute the injection energy and lower the injection temperature. This maximum injection temperature prevents extremely high temperatures which can cause computational problems (Gabor & Bournaud 2013).

As noted in Gabor & Bournaud (2013), numerous tests show that black holes sometimes scatter from the centres of their host galaxies by hundreds of pc. In merger simulations, the scattering is even more pronounced. Some of this scattering is a numerical artifact – it essentially does not occur in the GASOLINE simulations (except on small scales, which can be reduced with improved dynamical friction modeling; see Tremmel et al. 2015). The scattering in RAMSES is reduced, but not eliminated, when a more accurate direct-summation N-body gravity solver is applied to the sink particle (cf. Bleuler & Teyssier 2014). On the

other hand, some scattering (at the  $\sim 10^2$  pc level) is physically realistic given the dynamics in the nucleus (see §3.2.4 for additional discussion). To limit scattering, we adopt a well-known solution of assigning a black hole dynamical mass that is much larger than the true mass (e.g. Debuhr et al. 2010). For the gravity calculation, the black hole is assigned a mass of  $10^9 M_{\odot}$ , while we use the true mass for black hole-specific physics (e.g. Bondi accretion). This effectively keeps the black holes in their galactic centers by increasing the dynamical friction due to stars and dark matter.

### 2.2.1. RAMSES simulation set up and initial conditions

Initial conditions for the RAMSES simulations are generated separately from those for the GASOLINE runs, following the description in Gabor & Bournaud (2013). We use the same masses, density profiles and numbers of particles (for stars and for dark matter) as in the GASOLINE simulations, and initialize the positions and velocity distributions with the Cartesian grid code from Bournaud & Combes (2002).

The initial conditions generator determines equilibrium positions and phase-space velocity distributions for stellar and dark matter particles, taking into account the gas disk contribution to the gravitational potential, and the gas density distribution if initialized analytically in RAMSES. We also must initialize gas cells outside the disk: technically, null densities could not be handled properly. We do this by setting their density very low ( $\sim 10^{-7} \text{ cm}^{-3}$ ) so that the initial contribution to the circumgalactic halo is marginal: this halo will form from outflows during the simulation. Supermassive black holes are added to the galactic centers at the start of the RAMSES runs.

A necessary difference with the GASOLINE initial conditions is that the dark matter halo must be truncated to fit within the chosen simulation box size. The truncation radius, depending on the halo and box sizes, is 70 to 85% of the virial radius  $R_{200}$ . To maintain the halo truncation over time, we truncated the Maxwellian distribution of velocities for dark matter particles at 90% of the local escape velocity (computed at the initial position of each particle), otherwise the halo expands spatially over time and dynamically evaporates from the RAMSES simulation box. When truncating the haloes, we made the choice to keep the same total halo mass, so at very large separations during the early phases of the interaction the two galaxies have the same total masses and keep similar orbits with the two codes, and undergo their collision under nearly identical configurations. Yet at lower separations once the systems start to overlap the halo densities start to differ: haloes generated this way end up with slightly higher masses within  $R_{200}$  and smaller radii than the GASOLINE haloes (by a few percent typically), so short-range gravity and dynamical friction are somewhat stronger in the RAMSES simulations. This will be discussed later when comparing the detailed evolution of each merging system.

As in the GASOLINE case, we wish for each galaxy to undergo a relaxation period of  $\sim 100$  Myr. We do not have a simple method to insert a fully relaxed galaxy into a RAMSES merger simulation, so the relaxation must occur during the main simulation. Given our orbital parameters, the galaxies remain quasi-isolated and undisturbed by tidal forces during the first 200 – 300 Myr of the merger, which is sufficient to allow relaxation (1-2 disk dynamical times) and allow the formation of internal features such as bars and spiral arms before the interaction itself occurs.

For the merger, galaxies begin with the same orbital parameters (initial separation and velocities) and orientations (prograde-

prograde) as in the GASOLINE simulations. As noted above, the mergers evolve in a cubic box with a size of 250 kpc.

## 3. Results

### 3.1. General behaviour: common features

Figure 1 presents face-on images of gas surface density in our 4:1 RAMSES and GASOLINE simulations. First we show first apocenter, then a zoom-in of the primary galaxy at the same snapshot, and finally the merging galaxies at second pericenter. In Figure 2 we compare the time evolution of various quantities during a 4:1 merger in our GASOLINE and RAMSES simulations. At the top, we show the separation between the primary and secondary black holes. Below the separation plots, separately for the primary and secondary, we show the black hole accretion rates (BHARs), gas masses within 1 kpc of the black hole, and SFRs within 1 kpc of the black hole. For the last two, we show e.g. the gas mass within spheres of five different radii, equally spaced from 200 pc to 1000 pc. Careful comparison of the RAMSES and GASOLINE snapshots in Figure 1 and in the top panels of Figure 2 indicates some differences in the galaxy orbits (e.g. in RAMSES the galaxies are farther apart at first apocenter), and differences in gas structures (e.g. in GASOLINE gas forms into smaller clouds). We will address these differences in §3.2.

Overall, however, the dynamics of the black holes is similar until we can follow them in a consistent way. We note here that in our GASOLINE simulations the black holes never merge, whereas in RAMSES they merge when the galaxies coalesce, shortly after third pericenter, once they pass within each others' accretion radii (in this case about 60 pc). Black hole mergers are implemented in GASOLINE, but we chose to turn them off to study the dynamical behavior (Van Wassenhove et al. 2014; Capelo et al. 2015). This choice affects accretion on the black holes, and therefore we refrain from commenting on black hole growth at late times in the simulation.

The patterns in star formation and black hole accretion driven by dynamics, i.e., how merger-driven inflows at pericenters enhance them, are also similar, once the differences in the orbits are taken into account. Indeed, one of the main conclusions of our experiment is that even when trying to make the set-up of our simulations as close as possible in the initial conditions and in the choices of implementations, the way parameters are set up is intrinsically different, and therefore differences arise even in a controlled experiment.

Qualitatively, the behavior in GASOLINE and RAMSES simulations is similar. At first pericenter, the black holes pass within about 10 kpc of each other, but this induces little gas inflow and little change in the BHARs or SFRs. Between first and second pericenter, the galaxies act essentially as though they are isolated, with relatively steady SFRs and BHARs. During this time the SFRs and especially the BHARs fluctuate on short timescales – in the BHAR case, fluctuations of an order of magnitude are common. These fluctuations result from stochastic fueling of the central black hole (Hopkins & Hernquist 2006), driven both by structure in the interstellar medium (ISM) and by AGN feedback (Gabor & Bournaud 2013). Following Capelo et al. (2015), we call this the stochastic phase of the merger.

The action begins at second pericenter. As the two black holes pass within a few kpc, tidal torques trigger an increase in gas mass within the central few hundred pc in both the primary and secondary galaxies. The central gas mass increase, more pronounced in the secondary, triggers enhanced central star formation and black hole growth. At third pericenter  $\sim 150$  Myr later,

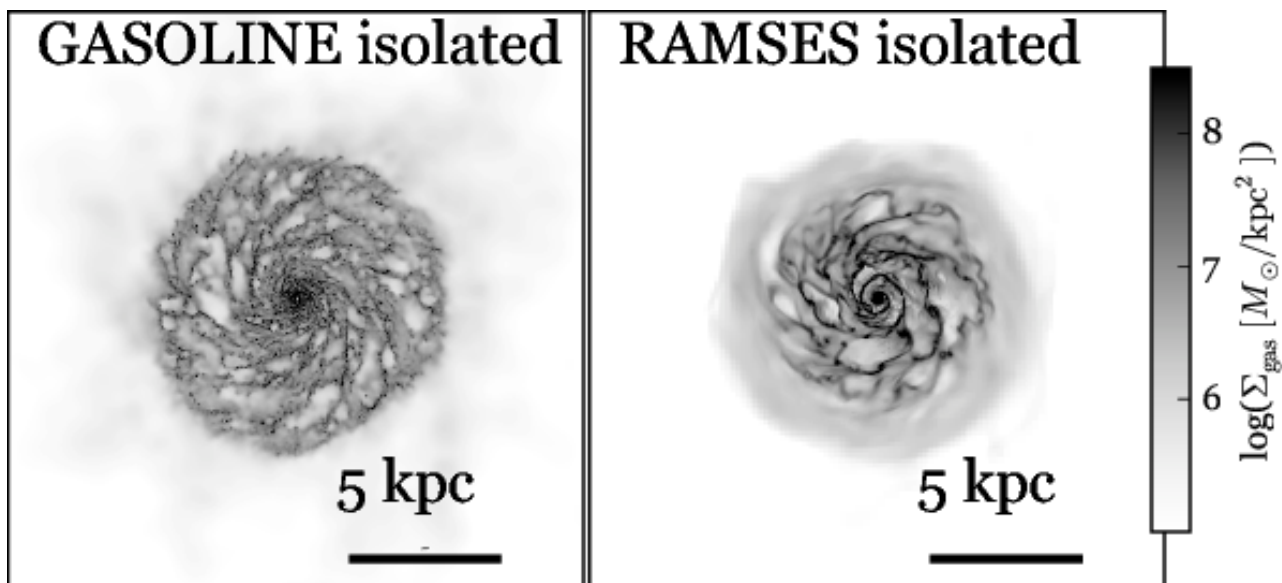


**Fig. 3.** Face-on images of gas surface density of an isolated disk galaxy simulation, using GASOLINE (left) and RAMSES (right). The characteristic sizes of gas structures are larger in RAMSES than in GASOLINE. This owes partly to the Jeans polytropic pressure floor implemented in RAMSES, and partly to differences in more fundamental aspects of the codes (e.g. hydrodynamic or gravity solvers).

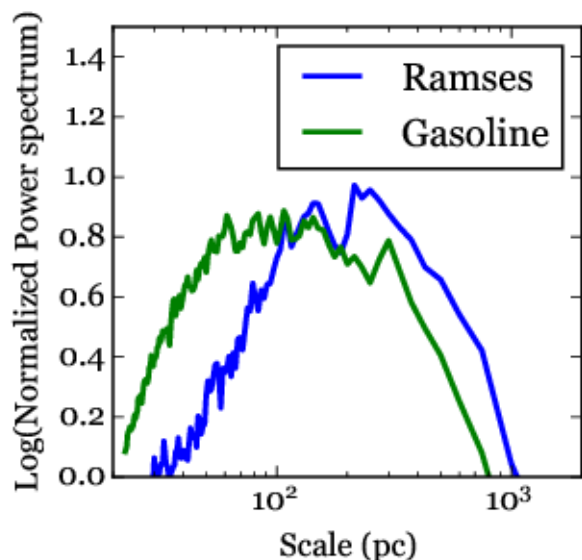


**Fig. 4.** Power spectra of gas surface density fluctuations in isolated GASOLINE and RAMSES galaxies. The power spectra are normalized by a third-degree power law to highlight the differences between simulations. GASOLINE shows more power at small scales, and less power at large scales, emphasizing that gas structures in our GASOLINE simulations tend to have smaller sizes than those in RAMSES.

the interaction induces another burst of activity. In both simulations, this picture (starting at second pericenter) roughly follows the well-known scenario of merger-driven starburst and AGN fueling (Sanders et al. 1988; Barnes & Hernquist 1991; Di Matteo et al. 2005).

In summary, the overall behavior of the RAMSES and GASOLINE simulations is similar, and broadly consistent with previous studies of galaxy mergers. There are, however, important discrepancies between the two simulations, which we address next. Understanding these differences and why they arise is important in order to extract and retain the results that we can consider robust.

## 3.2. Quantitative discrepancies

### 3.2.1. Orbits

The galaxy orbits differ slightly between the GASOLINE and RAMSES runs, as implied by the top panels of Figure 2. In the GASOLINE run, the galaxies move to wider separations between first and second pericentric passages (around  $t = 500$  Myr), and the second pericenter occurs at a later time ( $\sim 1.0$  Gyr rather than  $\sim 0.8$  Gyr in the RAMSES case). Since the mergers are initialized with the same positions and velocities in both simulations, we attribute these differences to mass discrepancies.

As described in §2, galaxy halos in RAMSES simulations must be truncated to fit inside a computationally reasonable box size. When we created the initial conditions, we chose to keep the total halo mass constant, so the truncation increases the dark matter density by a few percent inside the truncation radius. If instead we had kept the central density constant, then the total halo mass would be modified and the interaction orbit would start to differ even at large separations, before the two galaxies overlap or develop tidal features. Instead, our choice keeps the early-stage configuration of the interaction relatively unchanged (see Figure 1). Subsequently, the higher central density of the truncated RAMSES halo increases the gravitational forces at shorter distances, once the two haloes start to significantly overlap. We attribute the faster merging in RAMSES to this difference, rather than to effects of the codes themselves (e.g., Poisson solver type or accuracy). To further probe this, we estimated analytically the timescale required to “free-fall” from the first apocenter to the next encounter at  $\leq 5$  kpc, assuming the radial profile of the haloes and baryonic components did not evolve from the initial conditions: the timescales are 382 Myr for the GASOLINE initial mass distribution, and 327 Myr for the RAMSES one. The timescales measured in the simulations are about 350 and 290 Myr, respectively: they are both shorter than our analytic estimates (probably due to the extra effects of dynamical friction, and/or increased mass concentration at the first pericenter), but the relative difference of  $\approx 15\%$  is fully consistent with that in the analytical estimate. Hence, the faster merging timescale in the RAMSES merger is fully consistent with having resulted from our choice of keeping the total halo

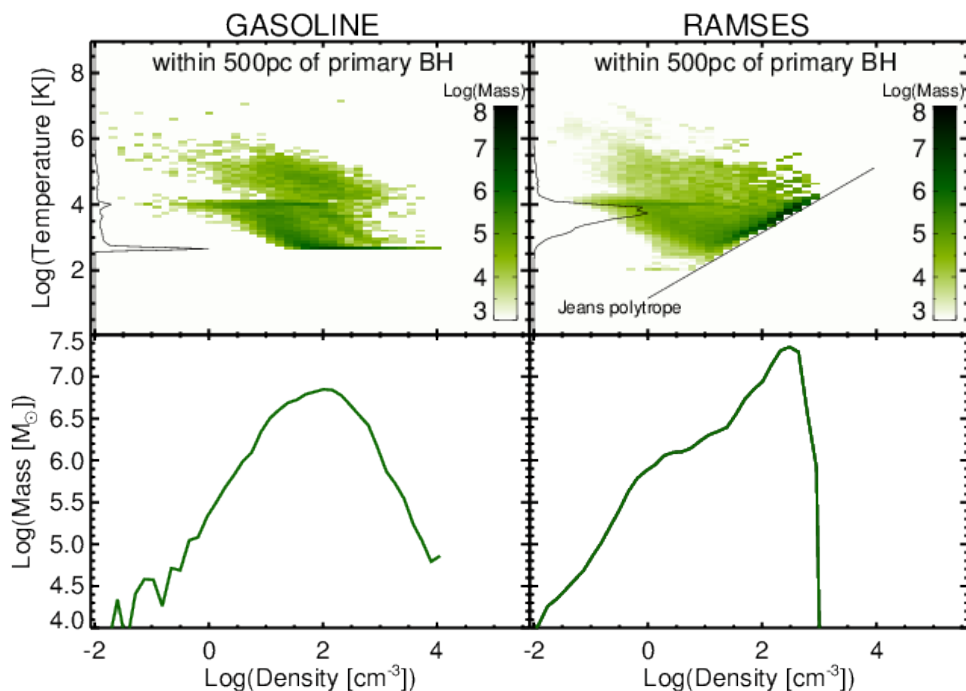


**Fig. 5.** Density-Temperature diagrams (**top row**) and density PDFs (**bottom row**) for gas in GASOLINE (**left column**) and RAMSES (**right column**). We show only gas within 500 pc of the primary galactic center in each simulation, and we use a snapshot near the maximum separation (first apocenter, around 500 Myr). In the top panels, we include the temperature distribution along the left axis (arbitrarily normalized, and shown on a linear scale). We also schematically show the Jeans polytrope temperature floor for the RAMSES simulation (straight black line), which keeps the average gas significantly hotter than in GASOLINE.

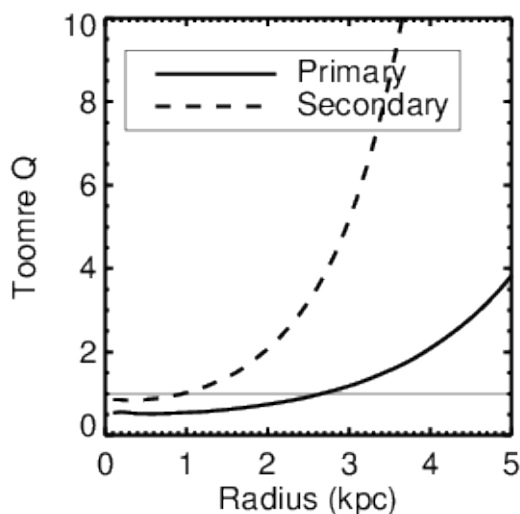


**Fig. 6.** Toomre  $Q$  parameter estimated as a function of radius for the initial disk galaxies in a 4:1 merger in RAMSES. A horizontal line marks the marginally-stable value  $Q = 1$ . At a gas temperature of  $10^3$  K (which is effectively enforced by the Jeans polytrope temperature minimum), the secondary galaxy is substantially more stable than the primary, and it remains stable or near marginal stability at all radii. This leads to a low SFR in the secondary. In the GASOLINE simulations without a Jeans polytrope, the secondary has higher SFRs.

mass constant when a truncation is applied to the initial conditions.

### 3.2.2. Black hole accretion rates

During the relatively quiescent phase between first and second pericenter, the BHARs differ significantly in the two simulations (see Figure 2): RAMSES BHARs fluctuate around  $10^{-4.5} M_{\odot} \text{ yr}^{-1}$ , while those in GASOLINE fluctuate around  $10^{-3.5} M_{\odot} \text{ yr}^{-1}$ . In any case, the black hole growth during this period is small because the accretion rates are low. Thus the detailed level of black hole fueling is relatively unimportant during the quiescent phase.

During the merger phase, the primary BHs show marked differences in the BHAR. In GASOLINE, the primary BHAR peaks sharply (by a factor  $> 10$ ) just after second pericenter, remains elevated (with large fluctuations) more-or-less until third pericenter, and rises again just after third pericenter. In RAMSES, the primary shows a brief spike in BHAR at second pericenter, then returns to the quiescent level even through third pericenter, until experiencing another spike at coalescence. The secondary BHARs, in contrast, are similar in both simulations, showing a peak in BHAR at second pericenter and another peak at third pericenter that lasts through coalescence. In RAMSES, black hole coalescence occurs  $\sim 50$  Myr after third pericenter, whereas coalescence never occurs in GASOLINE. The coalescence limits dual black hole growth in the merger remnant.

We attribute these quantitative discrepancies between black hole growth in GASOLINE and RAMSES mainly to differences in the black hole fueling and feedback models. In GASOLINE, the accretion rate includes a boost factor of 3 to the formal Bondi rate, and the feedback coupling efficiency is set to a relatively low value of 0.1% (calibrated from idealized mergers and zoom simulations; Bellovary et al. 2013). Thermal energy from feedback is dumped into a single nearby particle at every timestep without any storage. In RAMSES, on the other hand, the accretion rate includes no boost factor, and the coupling efficiency is set to rel-

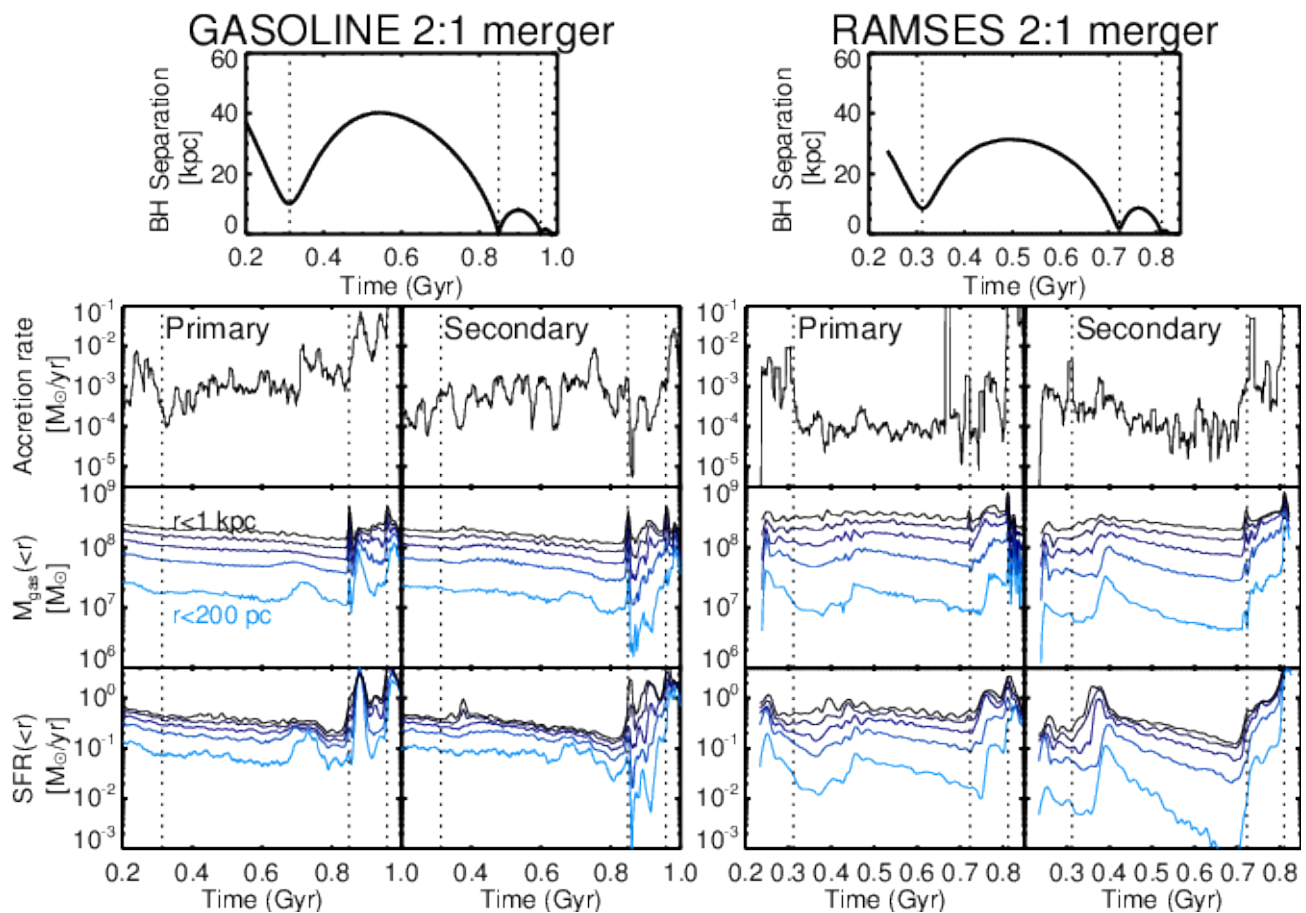


**Fig. 7.** Same as Figure 2, but for a 2:1 merger rather than a 4:1 merger. BH separation in kpc (top), BHAR in  $M_{\odot} \text{ yr}^{-1}$  (second row), gas mass in  $M_{\odot}$  within spheres up to 1 kpc in radius (third row), and SFR in  $M_{\odot} \text{ yr}^{-1}$  within the same spheres (bottom row) vs. time for a 2:1 merger with GASOLINE (left) and RAMSES (right). For each simulation, we show quantities for the primary galaxy/BH on the left, and the secondary galaxy/BH on the right. We show gas masses and SFRs within radii of 200 pc to 1 kpc, in increments of 200 pc. Vertical dotted lines mark local minima in the separation between the two black holes in all panels. The GASOLINE and RAMSES simulations show qualitatively similar results: enhanced accretion and star formation rates at second pericenter, and especially at 3rd pericenter/coalition.

atively high value of 0.15 (calibrated from cosmological simulations with much lower resolution, and slightly different feedback prescriptions; see Booth & Schaye 2009; Dubois et al. 2012). Feedback energy is dumped into the entire accretion region, but only if enough energy is “stored” to heat the gas in that region to  $10^7$  K, which increases the effective efficiency.

Black hole growth is mostly self-regulated in these simulations, suggesting that the difference in coupling efficiency causes more of a difference than the boost factor. The efficient feedback in RAMSES keeps the gas immediately around the black hole hot and diffuse, leading to lower accretion rates than in GASOLINE. This effect persists throughout both the stochastic phase and merger phase. Owing to the efficient feedback, bursts of accretion in RAMSES (see Figure 2) are short-lived and they drive only minor BH growth.

The implementation of supernova (SN) feedback in this set of RAMSES simulations may also contribute to suppressing black hole growth. Dubois et al. (2015) find that when the SN feedback implementation in RAMSES includes delayed cooling black hole growth is suppressed in galaxies with bulge mass below  $\sim 10^9 M_{\odot}$ , which is comparable to the bulge mass in our runs.

This BH growth discrepancy raises questions about the choice of AGN feedback efficiency. Our best method to calibrate the efficiency relies on comparing simulated black hole growth to observed BH demographics and  $M_{\text{BH}}$ -galaxy rela-

tions, especially  $M_{\text{BH}} - M_{\text{bulge}}$ . This was done using large-scale cosmological simulations for RAMSES, and idealized mergers and zoomed simulations for GASOLINE (Bellovary et al. 2013). Combined with the discrepancies in BH growth, this suggests that the optimal efficiency could depend on resolution (and stellar feedback effects). If so, this calibration could be especially problematic when pushing the boundaries of simulation resolution – it is computationally expensive to run several high-resolution simulations just for calibration.

In summary, different physical prescriptions for black hole fueling and feedback dominate over differences in hydrodynamic method (cf. Hayward et al. 2014). The efficient AGN feedback in RAMSES leads to lower BH accretion rates than in GASOLINE. The  $M_{\text{gas}}$  plots in Figure 2 – which show less gas inflow at late stages in RAMSES than in GASOLINE – suggest that gas dynamics play a role as well. In the next sections, we explore how the models for gas thermodynamics influence the gas structure of the galaxies, which in turn will influence the details of gas dynamics.

### 3.2.3. Galaxy gas structure

Figure 1 (especially the middle panels) suggests a key difference in gas structure between our RAMSES and GASOLINE simulations: gas forms larger, smoother structures in RAMSES. In order



to eliminate any possible effects of the galaxy merger, we compare these same primary galaxies but in an isolated context. We show images from these in Figure 3.

In the case of GASOLINE, we show a snapshot at 200 Myr of the 4:1 merger. This is well before the first pericenter, and thus the galaxy appears as it would in isolation. For the RAMSES case, we recall that the galaxies do not undergo a separate relaxation simulation before beginning the merger simulation, as do the GASOLINE galaxies. Thus the galaxies relax during the first 200–300 Myr before first pericenter. In order to make a fair comparison with the isolated GASOLINE galaxy, we ran a separate RAMSES simulation with an isolated version of the primary galaxy. We show a snapshot from this isolated RAMSES simulation at about 250 Myrs, which is similar to the “age” of the GASOLINE galaxy.

Figure 3 reinforces the difference in gas structure. In RAMSES the gas forms thick filaments and large clumps, whereas in GASOLINE the gas forms many smaller filaments and clouds, with a more flocculent appearance. Moreover, dense gas structures appear to extend to larger radii in GASOLINE, while the RAMSES outer disk is quite smooth.

To quantify the differences in gas structure, we calculate the power spectrum of two-dimensional spatial variations (as in Christensen et al. 2012). We first crop each gas surface density map shown in Figure 3 to a width of  $L \approx 6$  kpc to isolate the galaxy ISM, then calculate the 2D fast Fourier transform. This yields a 2D image in frequency space,  $\tilde{\Sigma}(u, v)$ , where  $u$  and  $v$  are frequency coordinates. We shift the image so that zero frequency is at the image center, and calculate the 2D power as  $P(u, v) = |\tilde{\Sigma}|^2$ . From the 2D power image we calculate the 1D power spectrum,  $P(k)$ , by calculating the average power per pixel in a concentric set of circular annuli. Here,  $k$  refers to the radius, in pixels, of each annulus placed on the frequency-space image;  $k$  is a spatial frequency coordinate related to spatial wavelength  $\lambda$  via  $\lambda = L/k$ . Structures of size  $s$  correspond to a wavelength of  $\lambda = 2s$ . Finally, we normalize the power spectrum by a power law to clarify the differences between simulations: in Figure 4 we show  $P'(s) = P(s)/(0.024s^3)$ . A third-degree power law roughly fits the shape of  $P(s)$ , so this normalization flattens the trend.

Figure 4 shows that our GASOLINE simulation has more power than RAMSES on scales  $s$  smaller than  $\approx 100$  pc, and less power on scales larger than  $\sim 200$  pc. This confirms that the sizes of gas structures in GASOLINE indeed tend to be smaller than those in RAMSES. Both simulations have the same amount of power on scales  $\sim 100$ – $200$  pc, which is approximately the width of filaments and clumps in the RAMSES simulation (i.e. the Jeans length). The GASOLINE simulation includes structures of this size, but their internal fragmentation leads to the enhanced power on smaller scales.

In the following section, we argue that the relative excess of gas structure on large scales in RAMSES is due to the implementation of a Jeans polytrope, the pressure floor which stabilizes the gas (which is absent from the GASOLINE simulations).

### 3.2.4. Stabilization by the Jeans polytrope

In Figure 5, we show density-temperature diagrams and density distributions in both GASOLINE and RAMSES. We show only gas within 500 pc of the primary BH at a timestep during the stochastic phase, between first and second pericenter. This gas is representative of gas in the disk of the galaxy.

We also schematically show the Jeans polytrope in the RAMSES density-temperature diagram. By construction, gas in RAMSES is not allowed to fall below this line. In contrast, a signif-

icant amount of gas in GASOLINE exists at lower temperatures and higher densities than imposed by this floor in RAMSES. At the GASOLINE temperature floor of 500 K, gas at the threshold for star formation ( $100 \text{ cm}^{-3}$ ) is resolved by  $\approx 64$  gas particles (with poorer relative resolution with increasing gas density). We note that GASOLINE includes an option to use a Jeans polytrope, but it frequently goes unused in galaxy formation simulations (as here) – mainly because the cold dense gas to which it applies is always star forming gas, which is treated with a sub-grid star formation model.

The thermal pressure imposed by the effective density-dependent temperature floor in RAMSES helps stabilize the galaxy’s gas disk against gravitational collapse. Gas does not reach densities higher than about  $10^3 \text{ cm}^{-3}$ , whereas the high-density tail in GASOLINE, where the temperature floor is independent of density, reaches  $10^4 \text{ cm}^{-3}$  (bottom panels of Figure 5). The gas temperature distribution (along the left axis of the density-temperature diagram) in RAMSES has a broad peak around  $10^4$  K, while in GASOLINE it shows a bimodal structure: a small peak around  $10^4$  K, and a larger peak around 500 K (the temperature floor). In both simulations a substantial portion of the gas reaches the temperature floor, but in RAMSES the temperature floor is set by the Jeans polytrope.

The higher typical gas temperature in RAMSES implies a more pressurized ISM, and a larger Jeans length (and Jeans mass). The larger Jeans length naturally leads to larger collapsed structures, giving rise to the larger filaments and gas clumps seen in Figures 1 and 3. This is reflected by the relative enhancement of power at scales  $\geq 200$  pc in the gas power spectrum (Figure 4). The higher temperature in RAMSES also affects the overall disk stability, which we address in §3.2.5.

To test whether the Jeans polytrope is the main driver of differences in gas structure, we ran RAMSES simulations of an isolated galaxy without the Jeans polytrope, and repeated the power spectrum analysis of §3.2.3. In this case, the power discrepancy on scales  $\geq 200$  pc between RAMSES and GASOLINE disappears (not shown). This implies that the Jeans polytrope is enhancing large-scale power by increasing the Jeans length. The relative deficit of small scale power ( $\lesssim 200$  pc) in RAMSES, on the other hand, persists even without the Jeans polytrope pressure floor (and also with changes to feedback models). The small-scale discrepancy thus seems to arise from more fundamental aspects of the simulations: numerical diffusion between gas cells in RAMSES could smooth out small-scale perturbations, or differences in the gravity solvers could lead to different levels of clumping.

Large gaseous clumps in RAMSES can have masses  $> 10$  times the black hole mass. The largest of these clumps may also contribute to the black hole scattering discussed in §2.2. We have performed a simple analytical estimate of the scattering induced by the clumps on the black hole motion on one RAMSES output. We calculated the change in the black hole’s velocity both due to distant encounters (Binney & Tremaine 1987) and assuming a single impulsive scatter that conserves energy and momentum, thus obtaining a lower and upper limit to the dynamical effect. In the case we analyzed the ensemble of the clumps was not producing any strong effect, but a single large clump with a mass 200 times larger than the black hole, and very close to it ( $\sim 60$  pc), could, in principle, have imparted a kick sufficient to displace the BH from the center.

### 3.2.5. SFRs

Overall SFRs during the stochastic phase are similar in both simulations. In both cases, the total SFRs are dominated by those in

the primary galaxies. This dominance is more pronounced in the RAMSES simulation, as the SFR of the secondary galaxy is quite low (see Figure 2). Notably, the gas mass within 1 kpc is similar for the two simulations, implying that RAMSES has a lower star formation efficiency ( $\text{SFR}/M_{\text{gas}}$ ).

We attribute the abnormally low SFR in the secondary RAMSES galaxy – but not in the primary galaxy – to the pressure support provided by the Jeans polytrope. As described above, the Jeans polytrope acts as a minimum temperature that ensures the Jeans length is always resolved.

From Figure 5, the RAMSES gas density distribution peaks around  $\sim 10^2 \text{ cm}^{-3}$ , at which density the temperature floor is around  $10^3 \text{ K}$ . We can quantify the stability imposed using an analysis of the Toomre  $Q$  parameter (Toomre 1964). In a thin galactic disk, the value of  $Q$  quantifies the stability of the disk against gravitational collapse: small values indicate gravitational collapse, large values indicate stability, and  $Q \approx 1$  indicates marginal instability. We estimate  $Q$  as a function of radius using:

$$Q = \frac{\sqrt{2}v_{\text{circ}}c_s}{\pi G r \Sigma} \quad (1)$$

where  $v_{\text{circ}}/r$  is the orbital frequency,  $v_{\text{circ}}(r)$  is the circular velocity at radius  $r$ ,  $c_s$  is the gas thermal sound speed,  $G$  is the gravitational constant, and  $\Sigma$  is the gas surface density in the disk at  $r$ .<sup>1</sup> We calculate  $c_s$  assuming a gas temperature of  $10^3 \text{ K}$ , which is roughly the limit imposed by the Jeans polytrope in RAMSES.

Figure 6 shows  $Q$  as a function of radius for the initial galaxies in the 4:1 merger. The primary galaxy is Toomre-unstable within a radius of  $\sim 2.5 \text{ kpc}$ . The smaller, secondary galaxy is significantly more stable than the primary, and  $Q$  barely reaches below 1 (and only in the central kpc). Thus, the Jeans polytrope stabilizes the smaller gas disk, inhibiting gravitational collapse and star formation.

This stabilization may also help explain why the SFRs near the secondary black hole during the merger phase (after second pericenter) are lower in RAMSES than those in GASOLINE. The amount of gas within 1 kpc of the secondary BH is similar in both simulations, but the SFR is lower in RAMSES (see Figure 2). Another contributor to the stability at smaller radii could be the presence of the artificially-massive black hole, which would boost the circular velocity and therefore  $Q$ . In the primary galaxy, however, we see little evidence for a suppression of the SF efficiency in the central regions of the RAMSES simulation relative to the GASOLINE simulation, suggesting that the extra-massive black hole plays little role. Finally, efficient AGN feedback may help maintain the gas at higher temperatures, suppressing the SF efficiency.

Near the primary BH, at and after third pericenter, the gas inflow to the central kpc is more significant in GASOLINE than in RAMSES. This leads to a larger gas mass and stronger burst of SF in GASOLINE than in RAMSES (see Figure 2). The origin of this difference is unclear. It could result from differences in the dynamics around the black holes, or from the efficient AGN feedback in RAMSES that evacuates gas from the nuclear regions.

Another possible driver of differences in SFR could be the supernova feedback recipe. In GASOLINE, gas heated by supernovae is not allowed to cool for a time that depends on local gas conditions. In RAMSES, the cooling delay is fixed at 20 Myr. Supernova feedback helps regulate star formation, so different

SFRs could arise from these different implementations. The primary galaxies have similar SFRs during the stochastic phase of our simulations, so the different supernova feedback seems to have a minor effect.

In summary, the two simulations have similar SFRs overall, but the GASOLINE simulation shows more SF in the secondary galaxy and during the merger phase than does the RAMSES simulation. We attribute these differences to stabilization due to the Jeans polytrope in RAMSES. This temperature floor increases the gas stability against collapse, suppressing star formation.

### 3.3. A 2:1 merger

We show the results of a 2:1 galaxy merger in Figure 7. Broadly, the behavior is similar to that in the 4:1 galaxy merger. The black holes undergo a relatively quiescent stochastic phase of growth lasting until second pericenter, at which point gas inflows trigger more activity. The star formation rates follow a similar broad pattern: steady star formation until second pericenter, then a boost triggered by gas inflows.

In the RAMSES simulation, the BH accretion rates during the stochastic phase are again lower than in GASOLINE, owing to differences in the supernova and AGN feedback model. The RAMSES primary BH shows little enhancement of accretion at second pericenter, while the GASOLINE primary shows a burst just after second pericenter. At third pericenter, both simulations show a burst of accretion. The secondary BHs show the opposite trend: the GASOLINE secondary shows little enhancement at second pericenter, and the RAMSES secondary shows a brief burst at second pericenter.

The star formation rates are broadly consistent between the simulations. The secondary galaxy in this 2:1 merger is sufficiently unstable (owing to higher gas surface densities) in RAMSES to have comparable SFR during the stochastic phase to that in GASOLINE. Both simulations show SFR enhancements between first and second pericenter, but these occur at different times and locations in the two simulations. The GASOLINE primary shows an SFR enhancement about 200 Myr before second pericenter; the GASOLINE secondary shows an unusual SFR peak at around 1 kpc within 100 Myrs after first pericenter, then a weak central burst about 200 Myrs before second pericenter. In RAMSES, both the primary and secondary galaxies show SFR bursts about 100 Myr after first pericenter, but the secondary one is much stronger. SFR enhancements during the merger phase again appear stronger in the GASOLINE simulation, but the differences are less pronounced than in the 4:1 simulation.

## 4. Conclusion

We have compared galaxy merger simulations including black hole growth with RAMSES, an AMR code, and GASOLINE, an SPH code, to find what is robust against differences in the codes and their physics implementations. We ran a small suite of new RAMSES simulations and used GASOLINE simulations from a suite described in Capelo et al. (2015). In both cases, the simulations had a spatial resolution of  $\sim 20 \text{ pc}$  and mass resolution of  $\sim 5 \times 10^3 M_{\odot}$ , and included standard sub-grid recipes for gas cooling, star formation, supernova feedback, and black hole fueling and feedback.

The simulations show general agreement in their dynamical behavior, and the results are broadly in line with the long-standing picture of galaxy merger simulation evolution (cf. Di Matteo et al. 2005; Hopkins et al. 2006). Black hole growth is

<sup>1</sup> This estimate is accurate for flat rotation curves, for which the epicyclic frequency is  $\kappa = \sqrt{2}\Omega = \sqrt{2}v_{\text{circ}}/r$ . It is an under-estimate of  $Q$  in the central kpc or so of our simulations, where the rotation is rising.

relatively slow while the galaxies are well-separated, including the time between first and second pericenter. During this phase, black hole growth is driven by stochastic accretion (Hopkins & Hernquist 2006; Gabor & Bournaud 2013; Capelo et al. 2015), just as for isolated galaxies. Once the galaxies' effective radii overlap at second pericenter, tidal torques trigger gas inflows toward the nuclei. The activity is strongest when the galaxies finally coalesce (beginning at third pericenter). The inflowing gas, driven to higher densities, initiates peaks in the SFR and the black hole accretion rate.

While the general behavior of the galaxy mergers is similar, there are quantitative differences between simulations run with different codes. We attribute most of these discrepancies to differences in sub-grid cooling and feedback models, but effects of the hydrodynamic methods (SPH and AMR) or even gravity solvers (gravity tree and Particle Mesh) may play a role. In RAMSES simulations, nuclear black holes accrete significantly less than in GASOLINE, both while the galaxies are well-separated and during coalescence. This arises due to a higher feedback efficiency in RAMSES, which regulates the black hole growth at a lower level. Furthermore, the more efficient black hole feedback ensures that central star formation is lower in RAMSES during the merger and coalescence. Another difference between codes is the ISM gas structure: in GASOLINE gas forms small filaments and collapses into tiny dense knots, whereas in RAMSES gas forms thick filaments and large clumps. Gas structure differences owe partly to the inclusion of a Jeans polytropic pressure floor in RAMSES, though at the smallest scales they may be related to numerical methods.

While differences in hydrodynamic method are important in some regimes of galaxy evolution models (e.g. Hayward et al. 2014), we conclude that the most important differences arise in the treatment of baryonic physics (cf. Scannapieco et al. 2012). Future work will better address the effects of hydrodynamic method by making the baryonic physics treatments as similar as possible, but due to differences in code structure, this is not always possible.

Our study underscores that simulation codes that successfully reproduce a range of observables are robust at predicting the same general physical behaviour in galaxy mergers, however, one should be careful when comparing quantitatively one particular simulation to one given observable, as these can be model-dependent. The trends, on the other hand, are robust, and can be used to obtain physical insight.

## Acknowledgements

FG acknowledges support from grant AST-1410012 and NASA ATP13-0020. TQ acknowledges support from NSF award AST-1311956.

## References

- Agertz, O., Moore, B., Stadel, J., et al. 2007, *MNRAS*, 380, 963  
 Barnes, J. E. & Hernquist, L. 1996, *ApJ*, 471, 115  
 Barnes, J. E. & Hernquist, L. E. 1991, *ApJ*, 370, L65  
 Beck, A. M., Murante, G., Arth, A., et al. 2015, *ArXiv e-prints*  
 Bellovary, J., Brooks, A., Volonteri, M., et al. 2013, *ApJ*, 779, 136  
 Bellovary, J. M., Governato, F., Quinn, T. R., et al. 2010, *ApJ*, 721, L148  
 Benson, A. J. 2005, *MNRAS*, 358, 551  
 Berger, M. J. & Colella, P. 1989, *Journal of Computational Physics*, 82, 64  
 Binney, J. & Tremaine, S. 1987, *Galactic dynamics*  
 Bleuler, A. & Teyssier, R. 2014, *MNRAS*, 445, 4015  
 Bondi, H. 1952, *MNRAS*, 112, 195  
 Booth, C. M. & Schaye, J. 2009, *MNRAS*, 398, 53  
 Bournaud, F. & Combes, F. 2002, *A&A*, 392, 83  
 Capelo, P. R., Volonteri, M., Dotti, M., et al. 2015, *MNRAS*, 447, 2123  
 Christensen, C., Quinn, T., Governato, F., et al. 2012, *MNRAS*, 425, 3058  
 Crenshaw, D. M., Kraemer, S. B., & George, I. M. 2003, *ARA&A*, 41, 117  
 Croton, D. J., Springel, V., White, S. D. M., et al. 2006, *MNRAS*, 365, 11  
 Debuhr, J., Quataert, E., & Ma, C.-P. 2011, *MNRAS*, 412, 1341  
 Debuhr, J., Quataert, E., Ma, C.-P., & Hopkins, P. 2010, *MNRAS*, 406, L55  
 Di Matteo, T., Springel, V., & Hernquist, L. 2005, *Nature*, 433, 604  
 Dubois, Y., Devriendt, J., Slyz, A., & Teyssier, R. 2010, *MNRAS*, 409, 985  
 Dubois, Y., Devriendt, J., Slyz, A., & Teyssier, R. 2012, *MNRAS*, 420, 2662  
 Dubois, Y., Volonteri, M., Silk, J., et al. 2015, *ArXiv e-prints*  
 Fabian, A. C., Sanders, J. S., Ettori, S., et al. 2000, *MNRAS*, 318, L65  
 Gabor, J. M. & Bournaud, F. 2013, *MNRAS*, 434, 606  
 Gabor, J. M. & Bournaud, F. 2014, *MNRAS*, 437, L56  
 Gerhard, O. E. 1981, *MNRAS*, 197, 179  
 Gingold, R. A. & Monaghan, J. J. 1977, *MNRAS*, 181, 375  
 Hahn, O., Teyssier, R., & Carollo, C. M. 2010, *MNRAS*, 405, 274  
 Hayward, C. C., Torrey, P., Springel, V., Hernquist, L., & Vogelsberger, M. 2014, *MNRAS*, 442, 1992  
 Hernquist, L. 1989, *Nature*, 340, 687  
 Hernquist, L. 1990, *ApJ*, 356, 359  
 Hopkins, P. F. 2014, *ArXiv e-prints*  
 Hopkins, P. F. & Hernquist, L. 2006, *ApJS*, 166, 1  
 Hopkins, P. F., Hernquist, L., Cox, T. J., et al. 2006, *ApJS*, 163, 1  
 Katz, N. 1992, *ApJ*, 391, 502  
 Keller, B. W., Wadsley, J., Benincasa, S. M., & Couchman, H. M. P. 2014, *MNRAS*, 442, 3013  
 Kereš, D., Vogelsberger, M., Sijacki, D., Springel, V., & Hernquist, L. 2012, *MNRAS*, 425, 2027  
 Khochfar, S. & Burkert, A. 2006, *A&A*, 445, 403  
 Kim, J.-h., Abel, T., Agertz, O., et al. 2014, *ApJS*, 210, 14  
 Kim, J.-h., Wise, J. H., Alvarez, M. A., & Abel, T. 2011, *ApJ*, 738, 54  
 Kormendy, J. & Ho, L. C. 2013, *ARA&A*, 51, 511  
 Krumholz, M. R., McKee, C. F., & Klein, R. I. 2004, *ApJ*, 611, 399  
 Lucy, L. B. 1977, *AJ*, 82, 1013  
 Machacek, M. E., Bryan, G. L., & Abel, T. 2001, *ApJ*, 548, 509  
 Marconi, A. & Hunt, L. K. 2003, *ApJ*, 589, L21  
 Mihos, J. C. & Hernquist, L. 1996, *ApJ*, 464, 641  
 Navarro, J. F., Frenk, C. S., & White, S. D. M. 1996, *ApJ*, 462, 563  
 Negroponte, J. & White, S. D. M. 1983, *MNRAS*, 205, 1009  
 Nelson, D., Vogelsberger, M., Genel, S., et al. 2013, *MNRAS*, 429, 3353  
 Newton, R. D. A. & Kay, S. T. 2013, *MNRAS*, 434, 3606  
 Perret, V., Renaud, F., Epinat, B., et al. 2014, *A&A*, 562, A1  
 Randall, S. W., Forman, W. R., Giacintucci, S., et al. 2011, *ApJ*, 726, 86  
 Rupke, D. S. N. & Veilleux, S. 2011, *ApJ*, 729, L27  
 Sanders, D. B., Soifer, B. T., Elias, J. H., et al. 1988, *ApJ*, 325, 74  
 Scannapieco, C., Wadepuhl, M., Parry, O. H., et al. 2012, *MNRAS*, 423, 1726  
 Shen, S., Wadsley, J., & Stinson, G. 2010, *MNRAS*, 407, 1581  
 Silk, J. & Rees, M. J. 1998, *A&A*, 331, L1  
 Somerville, R. S., Hopkins, P. F., Cox, T. J., Robertson, B. E., & Hernquist, L. 2008, *MNRAS*, 391, 481  
 Springel, V. 2005, *MNRAS*, 364, 1105  
 Springel, V. 2010, *MNRAS*, 401, 791  
 Springel, V., Di Matteo, T., & Hernquist, L. 2005, *ApJ*, 620, L79  
 Springel, V. & White, S. D. M. 1999, *MNRAS*, 307, 162  
 Stadel, J. G. 2001, PhD thesis, UNIVERSITY OF WASHINGTON  
 Stinson, G., Seth, A., Katz, N., et al. 2006, *MNRAS*, 373, 1074  
 Teyssier, R. 2002, *A&A*, 385, 337  
 Teyssier, R., Moore, B., Martizzi, D., Dubois, Y., & Mayer, L. 2011, *MNRAS*, 414, 195  
 Teyssier, R., Pontzen, A., Dubois, Y., & Read, J. I. 2013, *MNRAS*, 429, 3068  
 Toomre, A. 1964, *ApJ*, 139, 1217  
 Toomre, A. & Toomre, J. 1972, *ApJ*, 178, 623  
 Tremmel, M., Governato, F., Volonteri, M., & Quinn, T. R. 2015, *MNRAS*, 451, 1868  
 Truelove, J. K., Klein, R. I., McKee, C. F., et al. 1997, *ApJ*, 489, L179  
 Van Wassenhove, S., Capelo, P. R., Volonteri, M., et al. 2014, *MNRAS*, 439, 474  
 Vogelsberger, M., Sijacki, D., Kereš, D., Springel, V., & Hernquist, L. 2012, *MNRAS*, 425, 3024  
 Voit, G. M. & Donahue, M. 2005, *ApJ*, 634, 955  
 Wadsley, J. W., Stadel, J., & Quinn, T. 2004, *New A*, 9, 137  
 Wadsley, J. W., Veeravalli, G., & Couchman, H. M. P. 2008, *MNRAS*, 387, 427  
 Wurster, J. & Thacker, R. J. 2013a, *MNRAS*, 431, 2513  
 Wurster, J. & Thacker, R. J. 2013b, *MNRAS*, 431, 539  
 Wyithe, J. S. B. & Loeb, A. 2003, *ApJ*, 595, 614